



Solid-State Hydrogen Storage Properties of Ti–V–Nb–Cr High-Entropy Alloys and the Associated Effects of Transitional Metals ($M = \text{Mn, Fe, Ni}$)

Bo Cheng^{1,2} · Yunkai Li² · Xiaoxi Li² · Huibin Ke² · Liang Wang³ · Tangqing Cao² · Di Wan⁴ · Benpeng Wang² · Yunfei Xue^{1,2}

Received: 28 December 2021 / Revised: 14 January 2022 / Accepted: 27 January 2022
© The Author(s) 2022

Abstract

Recently, high-entropy alloys (HEAs) designed by the concepts of unique entropy-stabilized mechanisms, started to attract widespread interests for their hydrogen storage properties. HEAs with body-centered cubic (BCC) structures present a high potential for hydrogen storage due to the high hydrogen-to-metal ratio (up to $H/M = 2$) and vastness of compositions. Although many studies reported rapid absorption kinetics, the investigation of hydrogen desorption is missing, especially in BCC HEAs. We have investigated the crystal structure, microstructure and hydrogen storage performance of a series of HEAs in the Ti–V–Nb–Cr system. Three types of TiVCrNb HEAs ($\text{Ti}_4\text{V}_3\text{NbCr}_2$, $\text{Ti}_3\text{V}_3\text{Nb}_2\text{Cr}_2$, $\text{Ti}_2\text{V}_3\text{Nb}_3\text{Cr}_2$) with close atomic radii and different valence electron concentrations (VECs) were designed with single BCC phase by CALPHAD method. The three alloys with fast hydrogen absorption kinetics reach the H/M ratio up to 2. Particularly, $\text{Ti}_4\text{V}_3\text{NbCr}_2$ alloy shows the hydrogen storage capacity of 3.7 wt%, higher than other HEAs ever reported. The dehydrogenation activation energy of HEAs' hydride has been proved to decrease with decreasing VEC, which may be due to the weakening of alloy atom and H atom. Moreover, $\text{Ti}_4\text{V}_3\text{NbCr}_2M$ ($M = \text{Mn, Fe, Ni}$) alloys were also synthesized to destabilize hydrides. The addition of Mn, Fe and Ni lead to precipitation of Laves phase, however, the kinetics did not improve further because of their own excellent hydrogen absorption. With increasing the content of Laves phase, there appear more pathways for hydrogen desorption so that the hydrides are more easily dissociated, which may provide new insights into how to achieve hydrogen desorption in BCC HEAs at room temperature.

Keywords High-entropy alloy · Hydrogen storage · CALPHAD · Hydride stability · Hydrogen sorption kinetics

1 Introduction

To meet the future global carbon emission reduction target, the development of clean and renewable energy like hydrogen has become the need of the hour. The safe, effective, and economical storage of hydrogen [1, 2] is a key link in the whole hydrogen economy. Among the three options (gas, liquid and solid) for hydrogen storage, the solid-state-based approach [3, 4] has been considered as one of the most promising ways for its high gravimetric and volumetric capacities and reasonable economics. Despite the fact that metal–organic frameworks (MOFs) [5, 6], carbon nanostructures [7, 8] and complex hydrides [9, 10] have shown an extraordinarily high storage capacity of above 10 wt%, there remains a lot of obstacles to overcome, such as poor cyclability, inadequate reversibility, and complex preparation. Based on the above concerns, hydrogen forms metal hydrides [11, 12] with certain metals and alloys which seems

Available online at <http://link.springer.com/journal/40195>.

- ✉ Di Wan
di.wan@ntnu.no
- ✉ Benpeng Wang
wangbenpeng@bit.edu.cn

- ¹ Yangtze Delta Region Academy of Beijing Institute of Technology, Jiaxing 314019, China
- ² School of Materials Science and Engineering, Beijing Institute of Technology, Beijing 100081, China
- ³ Institute of Advanced Structure Technology, Beijing Institute of Technology, Beijing 100081, China
- ⁴ Department of Mechanical and Industrial Engineering, Norwegian University of Science and Technology, 7491 Trondheim, Norway

to be a more feasible operation to realize hydrogen storage with low cost, improved cyclability, appropriate capacity and trustworthy safety. Recently, high-entropy alloys (HEAs), designed by the concepts of unique entropy-stabilized mechanism [13, 14], started to attract widespread interests for their hydrogen storage properties.

The first report on the application of high entropy alloys for hydrogen storage was in 2010. CoFeMnTiVZr HEA with C14 Laves phase [15] can absorb and desorb up to 1.6 wt% of H₂ at room temperature. The effect of the chemical composition of the alloy on H₂ storage is revealed from the lattice constant, elemental segregation and enthalpy of hydride formation. Similar HEAs with Laves phase structure [16] have been reported for hydrogen storage by alloys of CrFeMnTiVZr system. Activated by high temperature, the hydrogen storage capacity at room temperature observed was 1.85 wt%, with the desorption ratio was poor as 20%. In addition, Edalati et al. applied CALPHAD methods [17] in the design of hydrogen storage alloys. The designed alloy TiZrCrMnFeNi, with single-phase thermodynamic stability and valence electron concentration (VEC) of 6.4, absorbed and desorbed 1.7 wt% of hydrogen reversibly at room temperature without prior activation process in the first hydrogenation/dehydrogenation cycle. However, the hydrogen storage capacities reported so far for the investigated Laves-phase HEAs are limited to ~2 wt% with a hydrogen-to-metal ratio (*H/M*) of almost one due to the hydrogen occupation site [18–21].

Materials with body-centered cubic (BCC) structure are thought to be a high-capacity hydrogen storage alloy due to the fact that BCC structure is non-close-packed one with more interstitial sites for hydrogen occupancy [22]. Sahlberg et al. prepared the TiVZrNbHf HEA [23] in terms of *H/M* up to 2.5, where *H/M* was only 2 in conventional BCC alloys [24–26]. The subsequent in-situ neutron powder diffraction (NPD) demonstrated that hydrogen seems favorable to both octahedral and tetrahedral sites caused by large lattice strain [27]. Despite some controversy about hydrogen occupation [28–30], HEAs with BCC structure could have superior storage capacity. Other BCC-structure HEAs were also studied for hydrogen storage, such as TiZrNbHfTa [31], TiZrNbTa [32], TiVZrNb [33], TiZrHfMoNb [34]. All the alloys could be hydrogenated at an appropriate temperature after an activation procedure with *H/M* = 2, which competes with the well-researched Ti-V-Cr system [35–37]. Although the above studies reported rapid absorption kinetics and large capacity, it exhibits strong hydride stability, where desorption was attained only by applying temperatures higher than 623 K. Therefore, how to destabilize hydrides under moderate conditions is a key issue for BCC HEAs to become proper hydrogen storage materials.

Nygård et al. [38, 39] studied a series of HEAs with different elements and related the stability of its hydrides with

VEC. The addition of elements with more valence electrons leads to a decrease in the hydrogen release temperature. However, the effects on the lattice constant of the newly added elements are disregarded here, which would have a direct effect on the bond strength of metal-hydrogen in traditional BCC alloys [40–42]. Therefore, it is necessary to control the atomic radius and adjust the VEC within a defined system to examine its influence on hydride stability. In addition, the effect of the Laves phase [43, 44] should not be ignored. The presence of a predominant C14 Laves phase structure in HEAs has been reported to desorb hydrogen at room temperature [45], which implies that single BCC structure with secondary phases (such as Laves phase) may also lead to the destabilization of the hydride.

In the present work, Ti₄V₃NbCr₂, Ti₃V₃Nb₂Cr₂ and Ti₂V₃Nb₃Cr₂ alloys, which were designed with single BCC phase by CALPHAD, were prepared in nearly the same average-atomic-radius and differed VEC to examine the stability of hydrides. We confirmed that VEC is the key issue for the destabilization of HEAs-based hydride. The designed Ti₄V₃NbCr₂ alloy demonstrated an excellent performance with maximum hydrogen storage capacity of 3.7 wt%, exceeding all HEAs for hydrogen storage ever reported. Transitional metals (Fe, Mn, Ni) have been also added to the targeted alloy to examine the effect of precipitated Laves phases.

2 Experimental

Ti–V–Nb–Cr system was chosen for the current study due to two reasons: (i) single BCC phase with a range of composition ratios can be easily formed in the system, which provides a higher flexibility to study the effect; (ii) the TiVNbCr alloy with equi-molar ratio could be hydrogenated without heat activation. The thermodynamic calculations were conducted using the CALPHAD method with Thermo-calc software using TCHEA3 database as will be discussed later.

Ti, V, Nb with 99.99% purity and Cr, Mn, Fe, Ni with 99.9% purity were used for alloy manufacturing. All the Ti–V–Nb–Cr HEAs were fabricated by arc melting from pure elements under an Ar atmosphere, as well as the alloyed Ti₄V₃NbCr₂*M* (*M* = Fe, Mn, Ni). During the arc-melting process, the ingots were flipped upside down and remelted at least four times with a piece of Ti getter being employed to prevent potential oxygen contamination. After arc melting, the fabricated ingots were cut into 3 mm × 3 mm × 3 mm cubes and loaded into an in-house built Sieverts apparatus to measure the hydrogen storage capacity and kinetics. Before the hydrogen storage test, the reliability and accuracy were carefully calibrated with the standard samples of LaNi₅ and TiFe.

For crystal structure examination, X-ray diffractometer (XRD, Rigaku, Japan) with Cu $K\alpha$ radiation ($\lambda = 0.15406$ nm, 45 kV, 40 mA) was used to identify the phase structure of the samples. The XRD data were collected in the 2θ range of 20° – 90° with a 0.02° step increment at ambient temperature. The morphologies of the samples were observed by scanning electron microscopy (SEM, Hitachi, Japan) equipped with energy-dispersive X-ray spectroscopy (EDS) analysis.

The hydrogen desorption properties have been studied by differential scanning calorimetry (DSC). A ~ 100 mg sample was placed inside an alumina crucible equipped with a pierced lid. Thermal analysis was carried out in a high-purity Ar atmosphere, and the sample was heated to 540°C at a heating rate of $10^\circ\text{C}/\text{min}$, $8^\circ\text{C}/\text{min}$ and $5^\circ\text{C}/\text{min}$, respectively.

3 Results and Discussion

3.1 Calculation of Phase Diagrams in Ti–V–Nb–Cr System

Phase prediction is a critical step to design HEAs due to the complex interaction of multi-elements [46, 47]. By CALPHAD modelling, the phase formation of the investigated HEAs ($\text{Ti}_4\text{V}_3\text{NbCr}_2$, $\text{Ti}_3\text{V}_3\text{Nb}_2\text{Cr}_2$ and $\text{Ti}_2\text{V}_3\text{Nb}_3\text{Cr}_2$) was predicted through Thermo-Calc software and the TCHEA3 database, as shown in Fig. 1. The BCC phase of $\text{Ti}_4\text{V}_3\text{NbCr}_2$, $\text{Ti}_3\text{V}_3\text{Nb}_2\text{Cr}_2$ and $\text{Ti}_2\text{V}_3\text{Nb}_3\text{Cr}_2$ alloys starts to form at 1583°C , 1632°C and 1707°C , respectively, the complete at the solidus temperature of 1561°C , 1590°C and 1631°C . The single BCC phase of $\text{Ti}_4\text{V}_3\text{NbCr}_2$ is predicted to be in the temperature range of 520°C – 1561°C , and the HCP_A3 forms at a temperature below 520°C . The appearance of HCP_A3 phase is not surprising for $\text{Ti}_4\text{V}_3\text{NbCr}_2$ alloys rich in Ti and V elements, since the accepted binary Ti–V phase diagram [48] shows a large temperature range of HCP_A3

phase formation. Similar phase diagram can be found for $\text{Ti}_3\text{V}_3\text{Nb}_2\text{Cr}_2$ and $\text{Ti}_2\text{V}_3\text{Nb}_3\text{Cr}_2$ alloys with HCP_A3 phase replaced by C15_Laves phase, which is very common in the Ti–Nb–Cr system [49]. It should be noted that although the phase diagram predicts a slight content of second phase (HCP_A3 or C15_Laves) at low temperatures, the wide temperature range suggests a tendency for all alloys to form single-phase structures considering the melting cooling process.

3.2 Microstructure and XRD Phase

All backscattered electron (BSE) images of as-cast alloys show typical as-cast microstructure in Fig. 2. The grain sizes are large ($> 300\ \mu\text{m}$) and distinct grain boundaries are seen. Uneven contrast of the SEM image indicates different compositional distribution in dendritic and inter-dendritic regions due to segregation during solidification. The EDS analysis shows that the dendrites (brighter regions) are enriched with higher melting point elements of Nb, V, and the dark regions are heavily enriched with Ti, Cr. Although the production of hexagonal close-packed (HCP) or Laves phases was predicted by CALPHAD, no apparent contrast belonging to the impurity phases can be found for all the prepared alloys by BSE analysis. Rapid solidification has been generally considered as effective in suppressing the formation of intermetallic compounds [50], and therefore secondary phases are difficult to be formed in the actual melting process of the alloy. This is further validated by XRD, as detailed below.

The XRD patterns of the Ti–V–Nb–Cr series alloys are shown in Fig. 3a. The as-cast alloys are composed of single BCC structure. The lattice constants were calculated using JADE software by least square method based on Bragg's law, as listed in Table 1. According to the law of partial substitution of elements, if the crystal structure remains unchanged, the substitution of metallic elements in the alloy leads to variation of the corresponding lattice

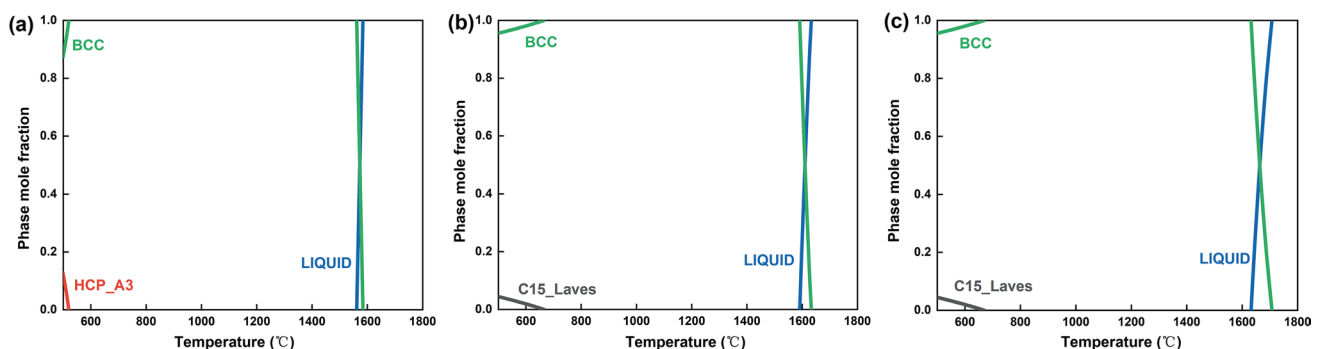


Fig. 1 Calculated phase diagram through Thermo-calc software and TCHEA3 database of **a** $\text{Ti}_4\text{V}_3\text{NbCr}_2$ alloy, **b** $\text{Ti}_3\text{V}_3\text{Nb}_2\text{Cr}_2$ alloys, **c** $\text{Ti}_2\text{V}_3\text{Nb}_3\text{Cr}_2$ alloy

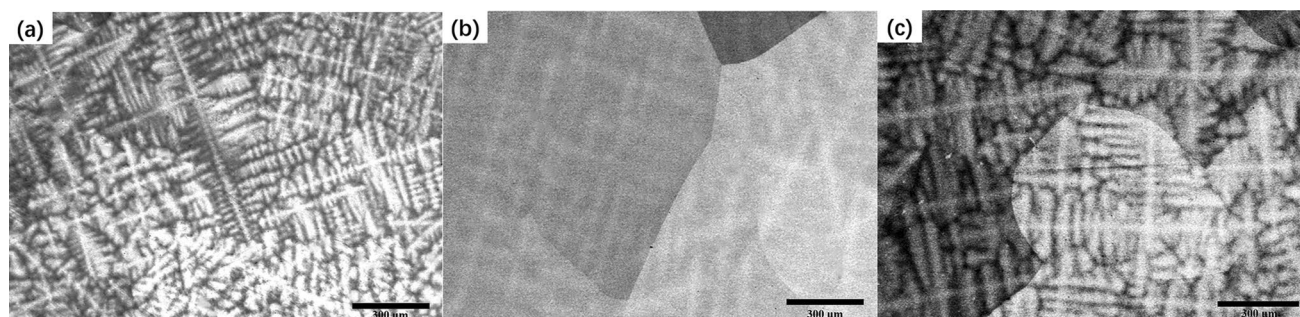


Fig. 2 BSE-SEM micrographs for **a** $\text{Ti}_4\text{V}_3\text{NbCr}_2$, **b** $\text{Ti}_3\text{V}_3\text{Nb}_2\text{Cr}_2$, **c** $\text{Ti}_2\text{V}_3\text{Nb}_3\text{Cr}_2$

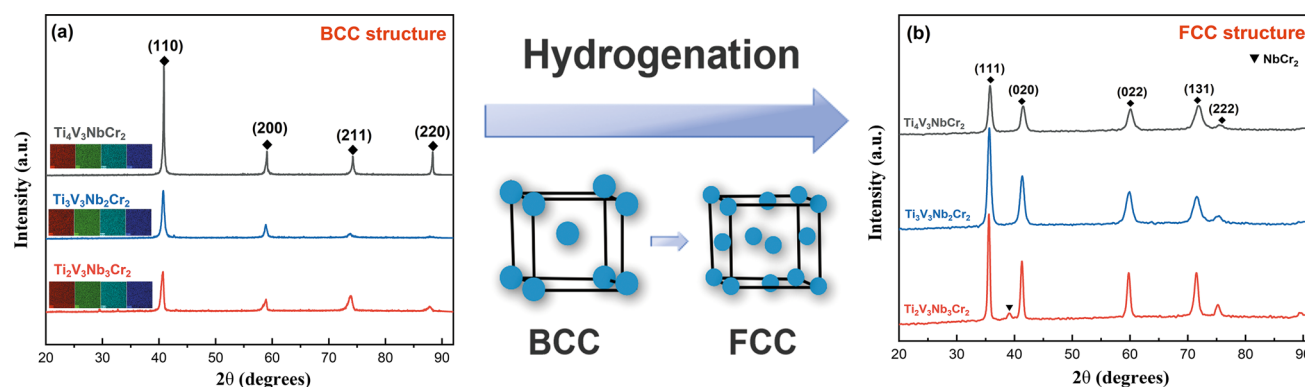


Fig. 3 XRD patterns of $\text{Ti}_4\text{V}_3\text{NbCr}_2$, $\text{Ti}_3\text{V}_3\text{Nb}_2\text{Cr}_2$ and $\text{Ti}_2\text{V}_3\text{Nb}_3\text{Cr}_2$ at initial as-cast state **a** and after hydrogen absorption **b**, respectively. Insets in **a** showing the element mapping using EDS of the arc-melted ingots

Table 1 Crystallographic data of Ti–V–Nb–Cr series alloys as designed

Alloys	VEC	Phase structure	Designed atom radius (Å)	Lattice parameters (Å)	Unit cell volume (Å ³)
$\text{Ti}_4\text{V}_3\text{NbCr}_2$	4.8	BCC	1.39	3.139	30.93
$\text{Ti}_3\text{V}_3\text{Nb}_2\text{Cr}_2$	4.9	BCC	1.39	3.135	30.81
$\text{Ti}_2\text{V}_3\text{Nb}_3\text{Cr}_2$	5	BCC	1.39	3.142	31.01

parameters as well as the cell volume. Thus, the crystallographic parameters remain constant mainly caused by the partial substitution of Ti (atomic radius: 147 pm) with Nb (146 pm) in the Ti–V–Nb–Cr series alloys as expected. Furthermore, Fig. 3a inset shows the element mapping using EDS of the arc-melted ingots in $\text{Ti}_4\text{V}_3\text{NbCr}_2$, $\text{Ti}_3\text{V}_3\text{Nb}_2\text{Cr}_2$ and $\text{Ti}_2\text{V}_3\text{Nb}_3\text{Cr}_2$, where no apparent elemental segregation was detected. Together with the above BSE micrographs, it can be concluded that three alloys with homogeneous elemental distribution and single-BCC phase as well as similar crystallographic parameters were well fabricated in the present study.

3.3 Hydrogen Storage Properties

It has been reported that TiVCrNb alloys [38] could be hydrogenated with no activation procedure but an incubation time of 360 min. Herein, for the convenience of the test, the samples were kept under vacuum at 473 K for 30 min and subsequently annealed to 300 K for hydrogen charging tests with a maximum hydrogen pressure of 50 bar. The first hydrogenation curves of the three alloys are shown in Fig. 4a.

After less than 3 min of hydrogen absorption process, the $\text{Ti}_4\text{V}_3\text{NbCr}_2$, $\text{Ti}_3\text{V}_3\text{Nb}_2\text{Cr}_2$ and $\text{Ti}_2\text{V}_3\text{Nb}_3\text{Cr}_2$ alloy reached hydrogen equilibrium of 3.7 wt%, 3.4 wt% and

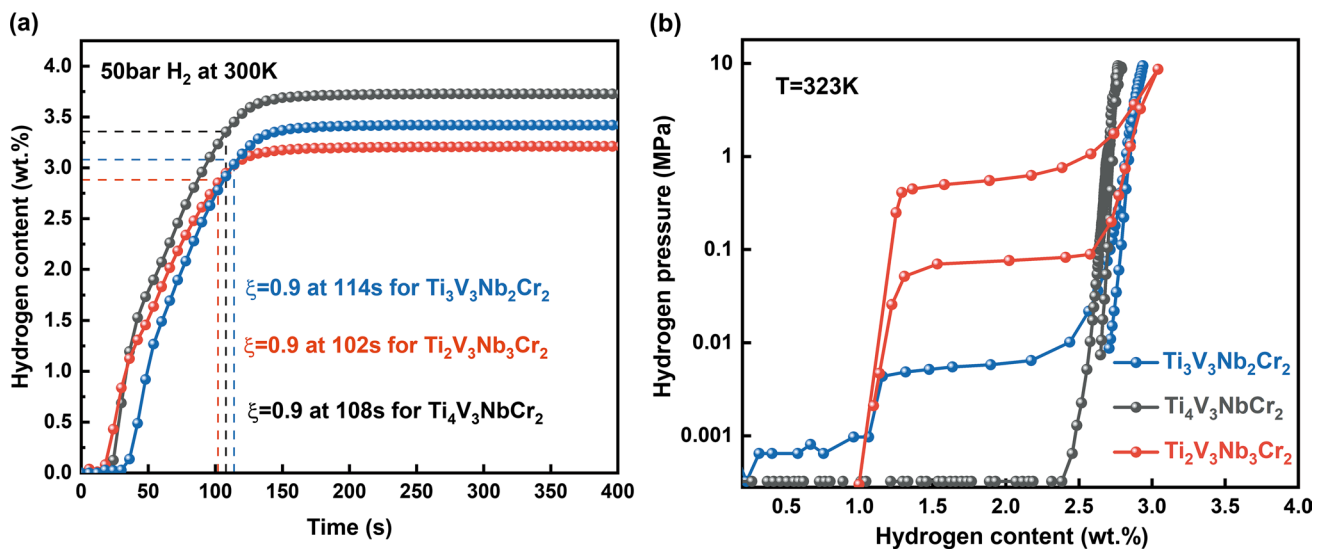


Fig. 4 **a** Hydrogen sorption kinetics of samples in the first cycle under 50 bar H_2 at 300 K, **b** PCT curves of the alloy samples after 1st cycle hydrogen absorption/desorption at 323 K

Table 2 Hydrogen storage properties of alloys

Alloys	Structure	Maximum capacity (wt%)	H/M
$Ti_4V_3NbCr_2$	BCC	3.7	2.01
$Ti_3V_3Nb_2Cr_2$	BCC	3.4	1.99
$Ti_2V_3Nb_3Cr_2$	BCC	3.2	2.02
$V_{55}Ti_{20.5}Cr_{18.1}Fe_{6.4}$ [52]	BCC	3.5	1.78
$TiV_{1.1}Mn_{0.9}$ [51]	BCC	2.99	1.53

3.2 wt%, respectively. Considering the molar masses of the corresponding alloys, the H/M obtained for all three are essentially equal to 2, which is much higher than that of the TiVMn [51] and TiVCr [52] alloys listed in Table 2. Such high values are not often seen in conventional BCC structures, where hydrogen usually occupies only tetrahedral sites. Sahlberg et al. [23] prepared TiVZrNbHf HEA with H/M as high as 2.5 and attributed this to the high lattice distortion in the HEA. However, TiVZrNb alloys with different Zr contents [33] were subsequently prepared to demonstrate that no correlation was observed between H/M and local lattice strain. Although controversy still exists, there is no doubt that H does occupy the tetrahedral and octahedral site of HEAs confirmed by in-situ XRD at different temperatures and in-situ and ex-situ neutron diffraction experiments [53]. Due to the above facts, the HEAs fabricated in the current work show large hydrogen storage capacities that have not been reported yet for similar alloys. It has also been exhibited in our work that arbitrary changes in composition can also be easily obtained with high H/M .

It has been known that hydrogen sorption kinetics directly affects its use for practical applications. The time taken to reach 90% of the maximum hydrogen uptake is usually used to examine the kinetics of hydrogen reaction [54]. It takes nearly 110 s to reach 90% of the hydrogen reacted fraction ($\xi=0.9$) for the three alloys, which is comparable to the rate in $LaNi_5$ alloys [55]. The possible limitations on the reaction rate [56–58] may be either: (a) the dissociation of hydrogen on the metal surface; or (b) H diffusion in the bulk; or finally: (c) hydride formation at the metal/hydride interface. Ni plays the role of catalyst [59] for hydrogen dissociation in $LaNi_5$, and thus fast kinetics is obtained. In the alloy of TiVNbCr HEAs, the fast kinetics matching those of $LaNi_5$ may be attributed to the catalytic effect of multi-principal elements [60] as well as the fact that more lattice defects induced by lattice distortion increase the nucleation rate of hydrides [54]. Moreover, there seems to be a slight difference in reaction kinetics between $Ti_4V_3NbCr_2$, $Ti_3V_3Nb_2Cr_2$ and $Ti_2V_3Nb_3Cr_2$ alloy. Discrepancies may arise from sample size or errors in the measurement system, which will be discussed in further work.

In addition, the structure of fully hydrogenated HEAs was analyzed by XRD, as shown in Fig. 3b. All the structures are highly similar to each other and are composed of FCC phase, except for the NbCr₂ phase separation found in $Ti_2V_3Nb_3Cr_2$ alloy. This mechanism in the hydrogenation from BCC to FCC phase is very common in HEAs and therefore will not be discussed in this study.

After the first hydrogenation, desorption is performed under high-temperature vacuum, followed by pressure-composition-temperature (PCT) testing. Figure 4b shows the PCT of the studied alloys at 323 K and up to 10 MPa.

From the PCT curve, the plateau of absorption and desorption under thermodynamic equilibrium conditions could be well evaluated. Two-plateau regions have been shown in the PCT curves, which are the typical characteristics for BCC alloys. The first plateau corresponds to the formation of a monohydride (solid-solution α -phase to β -phase) while the second plateau to the conversion to the dihydride (β -phase to γ -phase). Generally, the low plateau would reduce the usable hydrogen capacity by half when operated at working pressure. Although $\text{Ti}_{0.3}\text{V}_{0.25}\text{Zr}_{0.1}\text{Nb}_{0.25}\text{Ta}_{0.1}$ alloy [61] shows a single equilibrium pressure plateau below 0.1 MPa at 298 K, all the alloys studied here revealed two plateaus, which is in agreement with that reported by Shen et al. [62]. This would allow the alloy to bypass the two-stage absorption process thus allowing for complete dehydrogenation upon hydrogen release, which would make the HEA of great significance. However, there is still further research to be done regarding the hydrogen absorption mechanism of HEA in consideration of one-step and two-step hydrogenation. Herein, the first plateau was under very low plateau pressure. It was impractical to fully exhibit the reason at the moment since the current experimental setup has a limiting lower pressure of 0.1 kPa. The second equilibrium plateau of $\text{Ti}_4\text{V}_3\text{NbCr}_2$, $\text{Ti}_3\text{V}_3\text{Nb}_2\text{Cr}_2$ and $\text{Ti}_2\text{V}_3\text{Nb}_3\text{Cr}_2$ alloy was 0.6 MPa, 0.006 MPa and below 0.001 MPa, respectively. It is well-known that the equilibrium pressure is inversely related to the lattice constant [63]. The lattice constants of the three alloys are close to each other as mentioned above, and therefore, the change in equilibrium pressure cannot be explained by the volume. The equilibrium pressures are considered to have a correlation to the stability of hydrides. VEC value is regarded as a valid rule that is related to the stability of hydrides [38]: the larger VEC leads to the lower thermal stability of hydride phase. Since the VEC of $\text{Ti}_4\text{V}_3\text{NbCr}_2$, $\text{Ti}_3\text{V}_3\text{Nb}_2\text{Cr}_2$ and $\text{Ti}_2\text{V}_3\text{Nb}_3\text{Cr}_2$ alloy is 4.8, 4.9 and 5, respectively, the equilibrium pressures increase in the following order $\text{Ti}_2\text{V}_3\text{Nb}_3\text{Cr}_2 > \text{Ti}_3\text{V}_3\text{Nb}_2\text{Cr}_2 > \text{Ti}_4\text{V}_3\text{NbCr}_2$.

Whereas dehydrogenation is an endothermic reaction and hydrogen desorption of BCC solid solution requires a

relatively high temperature particularly. Herein, DSC was adopted to evaluate the hydrogen desorption performance for all HEAs studied. DSC curves were measured at different heating rates (5, 8, 10 K/min) under a continuous Ar flow from 273 to 673 K, as presented in Fig. 5. In order to minimize the errors, all tested alloys are in the saturated state under the hydrogen absorption conditions and tested in equal weight. As for hydrogen desorption, each curve has two endothermic peaks corresponding to the decomposition of hydrides. The first peak usually corresponds to the decomposition of the monohydride while the second corresponds to the decomposition of the dihydride, although only one peak exists in some room-temperature exothermic alloys such as $\text{Ti}_{27}\text{Cr}_{27}\text{V}_{40}\text{Fe}_6$ [64]. In addition, the peak temperature hysteresis is severe with an increasing heating rate. The DSC endothermic peak temperature of $\text{Ti}_4\text{V}_3\text{NbCr}_2$, $\text{Ti}_3\text{V}_3\text{Nb}_2\text{Cr}_2$ and $\text{Ti}_2\text{V}_3\text{Nb}_3\text{Cr}_2$ alloy is 708 K, 632 K and 509 K at 10 K/min heating rate, respectively. Obviously, the stability of hydrides is in the order of $\text{Ti}_2\text{V}_3\text{Nb}_3\text{Cr}_2 < \text{Ti}_3\text{V}_3\text{Nb}_2\text{Cr}_2 < \text{Ti}_4\text{V}_3\text{NbCr}_2$, as the VEC increases from 4.8 to 5. This implies that the hydride from the alloys with higher VEC releases hydrogen more easily. It has been reported that metal and H atoms interact positively and form strong bonds in metal hydrides [65]. The stability of such bonds is directly related to the Fermi energy level [66]: the lower the Fermi energy level, the higher the stability. The strong bond between alloy atom and H atom is weakened by the increase in the VEC, which explains the above-mentioned reduced desorption temperature.

The dehydrogenation activation energies can be estimated by the value of peak temperature at different heating rates based on the Kissinger formula [67], as is shown in follow:

$$\ln \left[\frac{k}{T_p^2} \right] = -\frac{E}{RT_p} + A, \quad (1)$$

where E is the activation energy of dehydrogenation, R is the gas constant (8.314 J/mol/K), T_p stands for the peak temperature, A is a linear constant and the temperature rate k has

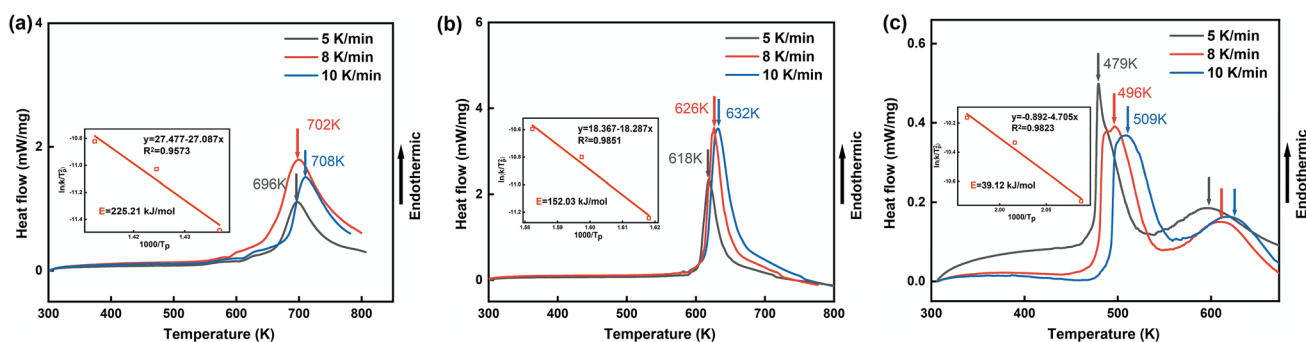


Fig. 5 DSC curves of hydrogenated alloys: **a** $\text{Ti}_4\text{V}_3\text{NbCr}_2$, **b** $\text{Ti}_3\text{V}_3\text{Nb}_2\text{Cr}_2$, **c** $\text{Ti}_2\text{V}_3\text{Nb}_3\text{Cr}_2$

been defined previously. Thus, the slopes in the plot of $\ln \left[\frac{k}{T_p^2} \right]$ and $1/T_p$ are utilized to calculate the value of the activation energy, as shown in Fig. 5 inset. The activation energy can be derived from their slopes, which are 225, 152 and 39 kJ/mol corresponding to the $\text{Ti}_4\text{V}_3\text{NbCr}_2$, $\text{Ti}_3\text{V}_3\text{Nb}_2\text{Cr}_2$ and $\text{Ti}_2\text{V}_3\text{Nb}_3\text{Cr}_2$ alloy. It is indicated that the activation energy of alloys decreased with the VEC and thus enhanced the desorption of hydrides.

3.4 Microstructure and XRD Pattern of $\text{Ti}_4\text{V}_3\text{NbCr}_2M$ ($M = \text{Mn, Fe, Ni}$) System

$\text{Ti}_4\text{V}_3\text{NbCr}_2$ shows a maximum capacity of 3.7 wt% H_2 that has exceeded all HEAs reported for hydrogen storage. It remains a problem that the hydride is too stable, making it difficult to release hydrogen. Herein, non-BCC forming elements (Mn, Fe and Ni) were added to the $\text{Ti}_4\text{V}_3\text{NbCr}_2$ alloy aimed at introducing new phases in BCC structure.

Figure 6a shows the XRD patterns of $\text{Ti}_4\text{V}_3\text{NbCr}_2M$ ($M = \text{Mn, Fe, Ni}$) alloys. It has been found that the phase structures of $\text{Ti}_4\text{V}_3\text{NbCr}_2M$ ($M = \text{Mn, Fe, Ni}$) alloys are determined as a single phase of BCC, except $\text{Ti}_4\text{V}_3\text{NbCr}_2\text{Ni}$. The addition of Fe and Mn elements leads to fewer precipitates than Ni, resulting in undetectable XRD patterns. The lattice constants of $\text{Ti}_4\text{V}_3\text{NbCr}_2\text{Mn}$, $\text{Ti}_4\text{V}_3\text{NbCr}_2\text{Fe}$ and

$\text{Ti}_4\text{V}_3\text{NbCr}_2\text{Ni}$ alloys are 0.4343 nm, 0.4315 nm, 0.4324 nm, respectively. The difference in lattice constants arises mainly from the radii of the doped atoms. The hydrogenation of the alloy follows the same pattern as that of the HEA described above with a phase transformation from BCC to FCC phase.

Microstructure for as-cast $\text{Ti}_4\text{V}_3\text{NbCr}_2M$ ($M = \text{Mn, Fe, Ni}$) alloys was studied by SEM, as shown in Fig. 6c–e. BCC phase and a small amount of impurity phase can be found in Fig. 6c, and the impurity phase is scattered within the crystal in the form of needle-like precipitates. It has been reported that the increment of Mn content in TiVMn alloy leads to the growth of C14_Laves phase [35]. EDS analyses were used to determine the elements distribution of the matrix and the precipitated phases, as listed in Table 3. The added Mn did not dissolve completely in the BCC matrix, but precipitated more into the Laves phase. The order of melting points of the elements is Nb (2750 K) > V/Cr (2183 K) > Ti (1941 K) > Mn (1519 K). According to the Gibbs function, the one with a higher melting point will nucleate preferentially, and therefore Nb, V, Cr, and Ti will solidify first in the liquid phase as BCC matrix. Subsequently the low melting point Mn will precipitate as Laves phase on the BCC matrix together with Ti, which leads to the enrichment of Ti, Mn elements in the Laves phase. A comparable interpretation could be also obtained in alloys of $\text{Ti}_4\text{V}_3\text{NbCr}_2\text{Fe}$ and $\text{Ti}_4\text{V}_3\text{NbCr}_2\text{Ni}$. Moreover, it can be seen that the addition

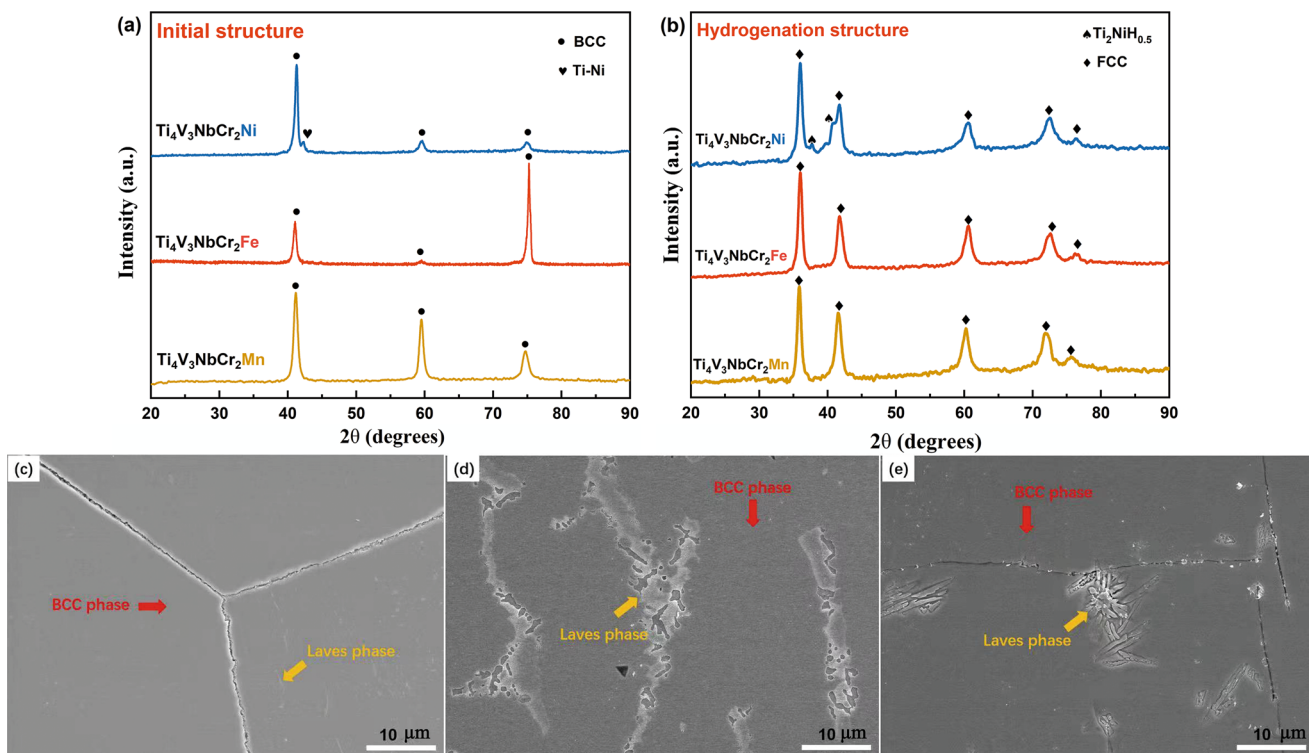


Fig. 6 XRD of $\text{Ti}_4\text{V}_3\text{NbCr}_2M$ ($M = \text{Mn, Fe, Ni}$) as-cast alloys **a** and its hydrides **b**, SEM micrographs for **c** $\text{Ti}_4\text{V}_3\text{NbCr}_2\text{Mn}$, **d** $\text{Ti}_4\text{V}_3\text{NbCr}_2\text{Fe}$, **e** $\text{Ti}_4\text{V}_3\text{NbCr}_2\text{Ni}$

Table 3 Elemental distribution (at.%) of the $\text{Ti}_4\text{V}_3\text{NbCr}_2\text{M}$ ($M=\text{Mn, Fe, Ni}$) alloys

Alloys	Phase	Ti	V	Nb	Cr	Mn	Fe	Ni
$\text{Ti}_4\text{V}_3\text{NbCr}_2\text{Mn}$	BCC	36.25	25.32	10.54	17.55	10.34	–	–
	Secondary phase	39.16	21.43	9.54	15.43	14.44	–	–
$\text{Ti}_4\text{V}_3\text{NbCr}_2\text{Fe}$	BCC	35.57	26.01	11.11	18.35	–	8.97	–
	Secondary phase	37.83	14.48	7.2	13.69	–	26.81	–
$\text{Ti}_4\text{V}_3\text{NbCr}_2\text{Ni}$	BCC	33.05	29.14	12.75	19.77	–	–	5.30
	Secondary phase	48.40	5.82	4.34	5.81	–	–	35.64

of Ni leads to the precipitation of more impurity phases, compared to Mn and Fe. This is in agreement with the XRD results, where the precipitates were labeled as TiNi phase. The formation of high entropy solid solutions also follows the traditional Hume-Rothery law, which requires that the miscible alloying elements have similar atomic sizes and electronegativity [68]. This means that large differences in atomic radii usually lead to the formation of intermetallic compounds. Compared to Fe and Mn elements, Ni has a larger difference in atomic radius with Ti, V, Cr, and Nb elements and therefore more secondary phases formed.

3.5 Hydrogen Storage Properties

The characterization of the hydrogen storage properties in $\text{Ti}_4\text{V}_3\text{NbCr}_2\text{M}$ ($M=\text{Mn, Fe, Ni}$) alloys is consistent with that of the HEAs described above, as shown in Fig. 7. The addition of alloying elements reduces the maximum hydrogen storage capacity to varying degrees. The $\text{Ti}_4\text{V}_3\text{NbCr}_2\text{Mn}$, $\text{Ti}_4\text{V}_3\text{NbCr}_2\text{Fe}$ and $\text{Ti}_4\text{V}_3\text{NbCr}_2\text{Ni}$ alloys reached hydrogen equilibrium of 3.65 wt%, 3.51 wt%, and 3.19 wt%, respectively. It has been reported that Laves phase precipitated at grain boundaries will act as a fast channel for hydride nucleation and thus enhance the kinetics of hydrogen absorption. Herein, Laves phase resulting from the addition of Fe, Mn, and Ni elements does not seem to accelerate the kinetics significantly, probably owing to the excellent hydrogen absorption kinetic characteristics of HEAs itself. Zhang et al. [54]

suggested that the lattice distortion of HEAs could induce more lattice defects (such as vacancies, dislocation, etc.), which will increase the nucleation rate of hydrides. And the apparent activation energy of hydrogen absorption in the HEA is even lower than that of LaNi_5 , thus exhibiting excellent hydrogen absorption kinetics. Therefore, although the improvement of hydrogen absorption kinetics by Laves phase is often applied to some kinetically slow conventional alloys, this strategy may not have a significant effect in HEAs.

As mentioned above, the $\text{Ti}_4\text{V}_3\text{NbCr}_2$ alloy has the hydrogen storage capacity of 3.7 wt% that has exceeded all HEAs reported. Limited by the strong bonds between metal and hydrogen atoms, it is difficult to desorb at room temperature. Fe, Mn, and Ni elements were added to the alloy with the expectation of reducing the stability of the hydride. Figure 7b shows the hydrogen absorption PCT curve of $\text{Ti}_4\text{V}_3\text{NbCr}_2\text{M}$ ($M=\text{Mn, Fe, Ni}$) alloys under 323 K. It is seen that the hydrogen absorption pressure of $\text{Ti}_4\text{V}_3\text{NbCr}_2\text{Mn}$, $\text{Ti}_4\text{V}_3\text{NbCr}_2\text{Fe}$ and $\text{Ti}_4\text{V}_3\text{NbCr}_2\text{Ni}$ alloys were 0.12 MPa, 0.16 MPa and 0.36 MPa, respectively. Compared to the plateau pressure below 0.001 MPa of $\text{Ti}_4\text{V}_3\text{NbCr}_2$ alloy, the addition of Fe, Mn and Ni elements significantly improves the hydrogen absorption plateau, indicating the decrease in stabilization of the hydrides. In the alloy of $\text{Ti}_4\text{V}_3\text{NbCr}_2\text{Ni}$, the most amount of secondary phase was precipitated. Laves hydrides are usually considered to desorb hydrogen at room temperature, and some

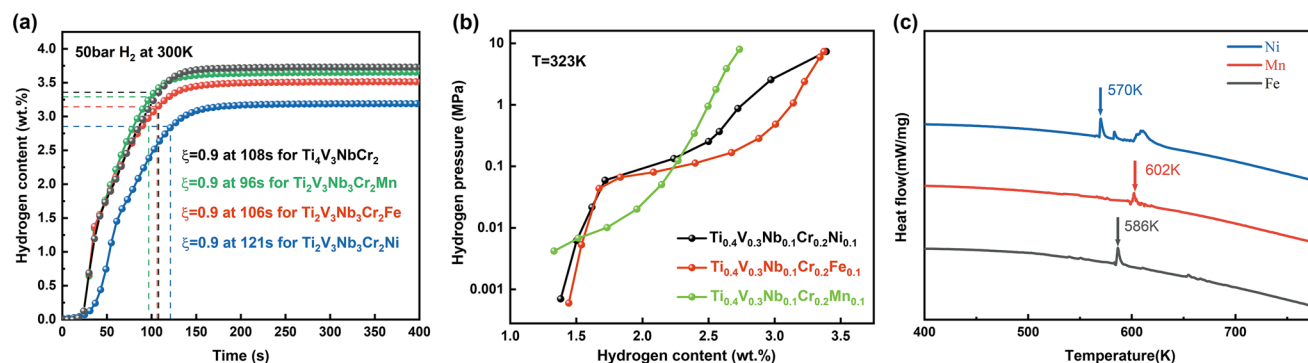


Fig. 7 **a** Hydrogen sorption kinetics of $\text{Ti}_4\text{V}_3\text{NbCr}_2\text{M}$ ($M=\text{Mn, Fe, Ni}$) alloys, **b** PCT curves of the alloy samples after 1st cycle hydrogen absorption/desorption at 323 K, **c** DSC curves of hydrogenated alloys at 10 K/min heating rate

single Laves-phase HEAs have been reported such as TiZrNbFeNi [45], TiZrCrMnFeNi [17]. In this article, Laves phase seems to play a role in reducing the hydride stability. More Laves phase precipitation leads to higher hydrogen uptake plateau pressure, which also means easier dissociation at room temperature. This can also be seen in the DSC curves, as shown in Fig. 7c. All the alloys can be dissociated at room temperature, so the first heat absorption peak referring to the dissociation of dihydride is usually not detected by DSC. The heat absorption peak on the DSC curves of $Ti_4V_3NbCr_2Mn$, $Ti_4V_3NbCr_2Fe$ and $Ti_4V_3NbCr_2Ni$ alloys were 602 K, 586 K and 570 K, respectively, which actually corresponds to the phase transition (from body-centered tetragonal/BCT to BCC) of monohydride. Therefore, it can be considered to be owing to its Laves phase which offers many pathways for hydrogen desorption so that the hydrides are more easily dissociated.

4 Conclusions

In this study, a series of HEAs in the TiVNbCr system were successfully designed by CALPHAD and fabricated by arc melting based on the designed compositions. The microstructure characteristics and the hydrogen storage performances were studied in explicit detail. The major conclusions are drawn as follows:

1. Three types of TiVCrNb HEAs ($Ti_4V_3NbCr_2$, $Ti_3V_3Nb_2Cr_2$, $Ti_2V_3Nb_3Cr_2$) with close atomic radii and different VEC were designed. It was found from XRD and SEM/EDS results that the as-cast alloys are BCC single phase.
2. $H/M=2$ was obtained for the designed alloys of different compositions, and composition fluctuations did not reduce this value. It is implied that HEAs can have great potential in terms of hydrogen storage capacity when lighter elements are selected. Particularly, $Ti_4V_3NbCr_2$ alloy shows the hydrogen storage capacity of 3.7 wt%, higher than other HEAs ever reported. Meanwhile, combined with the peak temperature from different DSC heating rates, the dehydrogenation activation energies of $Ti_4V_3NbCr_2$, $Ti_3V_3Nb_2Cr_2$ and $Ti_2V_3Nb_3Cr_2$ alloy using the Kissinger method were calculated to be 225 kJ/mol, 152 kJ/mol and 39 kJ/mol, respectively. It could be proved that the stability of hydrides decreases with VEC.
3. Transitional metals (Fe, Mn, Ni) have been further added to $Ti_4V_3NbCr_2$ alloy to destabilize hydrides. The addition of Ni leads to the most amount of Laves phase precipitation. Although the Laves phase in conventional alloys can improve the kinetics, this strategy does not seem to work in present HEAs because of their own

excellent hydrogen absorption. Furthermore, the addition of the Laves phase leads to a decrease in the desorption temperature.

Acknowledgements This work was financially supported by the National Natural Science Foundation of China (No. 51701018), the National Key Research and Development Program of China (No. 2018YFB0703400).

Funding Open access funding provided by NTNU Norwegian University of Science and Technology (incl St. Olavs Hospital - Trondheim University Hospital).

Declarations

Conflict of interest The authors state that there are no conflict of interest to disclose.

Open Access This article is licensed under a Creative Commons Attribution 4.0 International License, which permits use, sharing, adaptation, distribution and reproduction in any medium or format, as long as you give appropriate credit to the original author(s) and the source, provide a link to the Creative Commons licence, and indicate if changes were made. The images or other third party material in this article are included in the article's Creative Commons licence, unless indicated otherwise in a credit line to the material. If material is not included in the article's Creative Commons licence and your intended use is not permitted by statutory regulation or exceeds the permitted use, you will need to obtain permission directly from the copyright holder. To view a copy of this licence, visit <http://creativecommons.org/licenses/by/4.0/>.

References

- [1] Q.W. Lai, Y.H. Sun, T. Wang, P. Modi, C. Cazorla, U. Demirci, J.R.A. Fernandez, F. Leardini, K.F. Aguey-Zinsou, *Adv. Sust. Syst.* **3**, 1900043 (2019)
- [2] L. Schlapbach, *Nature* **460**, 809 (2009)
- [3] G. Principi, F. Agresti, A. Maddalena, S.L. Russo, *Energy* **34**, 2087 (2009)
- [4] K.L. Lim, H. Kazemian, Z. Yaakob, W.R.W. Daud, *Chem. Eng. Technol.* **33**, 213 (2010)
- [5] J.W. Ren, H.W. Langmi, B.C. North, M. Mathe, *Int. J. Energy Res.* **39**, 607 (2015)
- [6] N.L. Rosi, J. Eckert, M. Eddaoudi, D.T. Vodak, J. Kim, M. Okeffe, O.M. Yaghi, *Science* **300**, 1127 (2003)
- [7] A. Züttel, P. Sudan, Ph. Maurona, T. Kiyobayashi, Ch. Emmenegger, L. Schlapbach, *Int. J. Hydrogen Energy* **27**, 203 (2002)
- [8] M. Hirscher, M. Becher, M. Haluska, F.V. Zeppelin, X.H. Chen, U. Dettlaff-Weglikowska, S. Roth, *J. Alloys Compd.* **356**, 433 (2003)
- [9] I.P. Jain, P. Jain, A. Jain, *J. Alloys Compd.* **503**, 303 (2010)
- [10] M.B. Ley, L.H. Jepsen, Y.S. Lee, Y.W. Cho, J.M.B.V. Colbe, M. Dornheim, M. Rokni, J.O. Jensen, M. Sloth, Y. Filinchuk, J.E. Jørgensen, F. Besenbacher, T.R. Jensen, *Mater. Today* **17**, 122 (2014)
- [11] S.V. Alapati, J.K. Johnson, D.S. Sholl, *J. Phys. Chem. B* **110**, 8769 (2006)
- [12] N.A.A. Rusman, M. Dahari, *Int. J. Hydrogen Energy* **41**, 12108 (2016)
- [13] F. Marque, M. Balcerzak, F. Winkelmann, G. Zepon, M. Felderhoff, *Energy Environ. Sci.* **14**, 5191 (2021)

- [14] S. Akrami, P. Edalati, M. Fuji, K. Edalati, *Mater. Sci. Eng. R* **146**, 100644 (2021)
- [15] Y.F. Kao, S.K. Chen, J.H. Sheu, J.T. Lin, W.E. Lin, J.W. Yeh, S.J. Lin, T.H. Liou, C.W. Wang, *Int. J. Hydrogen Energy* **35**, 9046 (2010)
- [16] S.K. Chen, P.H. Lee, H. Lee, H.T. Su, *Mater. Chem. Phys.* **210**, 336 (2018)
- [17] P. Edalati, R. Floriano, A. Mohammadi, Y. Li, G. Zepon, H.W. Li, K. Edalati, *Scr. Mater.* **178**, 387 (2020)
- [18] R. Floriano, G. Zepon, K. Edalati, A. Mohammadi, *Int. J. Hydrogen Energy* **45**, 33759 (2020)
- [19] V. Zadorozhnyy, B. Sarac, E. Berdonosova, T. Karazehir, A. Lassnig, C. Gammer, M. Zadorozhnyy, S. Ketov, S. Klyamkin, J. Eckert, *Int. J. Hydrogen Energy* **45**, 5347 (2020)
- [20] B. Sarac, V. Zadorozhnyy, E. Berdonosova, Y.P. Ivanov, S. Klyamkin, S. Gumrukcu, A.S. Sarac, A. Korol, D. Semenov, M. Zadorozhnyy, A. Sharma, A.L. Greer, J. Eckert, *RSC Adv.* **10**, 24613 (2020)
- [21] I. Kunce, M. Polański, T. Czujko, *Int. J. Hydrogen Energy* **42**, 27154 (2014)
- [22] J.D. Li, X.Q. Yu, H.J. Zhao, H.Y. Shao, *Int. J. Hydrogen Energy* **44**, 29291 (2019)
- [23] M. Sahlberg, D. Karlsson, C. Zlotea, U. Jansson, *Sci. Rep.* **6**, 1 (2016)
- [24] G. Mazzolai, B. Coluzzi, A. Biscarini, F.M. Mazzolai, A. Tuissi, F. Agresti, S. Lo Russo, A. Maddalena, P. Palade, G. Principi, *J. Alloys Compd.* **466**, 133 (2008)
- [25] C.Y. Seo, J.H. Kim, P.S. Lee, J.Y. Lee, *J. Alloys Compd.* **348**, 252 (2003)
- [26] C. Iwakur, W.K. Choi, R. Miyauchi, H. Inoue, *J. Electrochem. Soc.* **147**, 2503 (2000)
- [27] D. Karlsson, G. Ek, J. Cedervall, C. Zlotea, K.T. Møller, T.C. Hansen, J. Bednarčík, M. Paskevicius, M.H. Sørby, T.R. Jensen, U. Jansson, M. Sahlberg, *Inorg. Chem.* **57**, 2103 (2018)
- [28] G. Ek, M.M. Nygård, A.F. Pavan, J. Montero, P.F. Henry, M.H. Sørby, M. Witman, V. Stavila, C. Zlotea, B.C. Hauback, M. Sahlberg, *Inorg. Chem.* **60**, 1124 (2020)
- [29] M.M. Nygård, Ø.S. Fjellvåg, M.H. Sørby, K. Sakaki, K. Ikeda, J. Armstrong, P. Vajeeston, W.A. Sławiński, H. Kim, A. Machida, Y. Nakamura, B.C. Hauback, *Acta Mater.* **205**, 116496 (2021)
- [30] J. Hu, J. Zhang, H. Xiao, L. Xie, H. Shen, P. Li, J. Zhang, H. Gong, X. Zu, *Inorg. Chem.* **59**, 9774 (2020)
- [31] C. Zlotea, M.A. Sow, G. Ek, J.P. Couzinié, L. Perrière, I. Guillot, J. Bourgon, K.T. Møller, T.R. Jensen, E. Akiba, M. Sahlberg, *J. Alloys Compd.* **775**, 667 (2018)
- [32] C. Zhang, A. Song, Y. Yuan, Y. Wu, P. Zhang, Z. Lu, X. Song, *Int. J. Hydrogen Energy* **45**, 5367 (2020)
- [33] M.M. Nygård, G. Ek, D. Karlsson, M. Sahlberg, M.H. Sørby, B.C. Hauback, *Int. J. Hydrogen Energy* **44**, 29140 (2019)
- [34] H. Shen, J. Zhang, J. Hu, J. Zhang, Y. Mao, H. Xiao, X. Zhou, X. Zu, *Nanomaterials* **9**, 248 (2019)
- [35] X.Y. Chen, R.R. Chen, X. Ding, H.Z. Fang, X.Z. Li, H.S. Ding, Y.Q. Su, J.J. Guo, H.Z. Fu, *Energy* **166**, 587 (2019)
- [36] S.W. Cho, C.S. Han, C.N. Park, E. Akiba, *J. Alloys Compd.* **288**, 294 (1999)
- [37] P. Ruz, S. Banerjee, R. Halder, A. Kumar, V. Sudarsan, *Int. J. Hydrogen Energy* **42**, 11482 (2017)
- [38] M.M. Nygård, G. Ek, D. Karlsson, M.H. Sørby, M. Sahlberg, B.C. Hauback, *Acta Mater.* **175**, 121 (2019)
- [39] B.H. Silva, C. Zlotea, Y. Champion, W.J. Botta, G. Zepon, *J. Alloys Compd.* **865**, 158767 (2021)
- [40] K. Sakaki, H.J. Kim, K. Asano, Y. Nakamura, *J. Alloys Compd.* **820**, 153399 (2020)
- [41] K. Kubo, H. Itoh, T. Takahashi, T. Ebisawa, T. Kabutomori, Y. Nakamura, E. Akiba, *J. Alloys Compd.* **356**, 452 (2003)
- [42] M. Okada, T. Chou, A. Kamegawa, T. Tamura, H. Takamura, A. Matsukawa, S. Yamashita, *J. Alloys Compd.* **356**, 480 (2003)
- [43] K. Young, J. Nei, D.F. Wong, L. Wang, *Int. J. Hydrogen Energy* **39**, 21489 (2014)
- [44] S. Banerjee, A. Kumar, P. Ruz, P. Sengupta, *Int. J. Hydrogen Energy* **41**, 18130 (2016)
- [45] R. Floriano, G. Zepon, K. Edalati, G.L.B.G. Fontana, A. Mohammadi, Z.L. Ma, H.W. Li, R.J. Contieri, *Int. J. Hydrogen Energy* **45**, 33759 (2020)
- [46] X.S. Huang, L.H. Liu, W.B. Liao, J.J. Huang, H.B. Sun, C.Y. Yu, *Acta Metall. Sin. -Engl. Lett.* **34**, 1546 (2021)
- [47] C. Xiang, Z.M. Zhang, H.M. Fu, E.H. Han, J.Q. Wang, H.F. Zhang, G.D. Hu, *Acta Metall. Sin. -Engl. Lett.* **32**, 1053 (2019)
- [48] J.L. Murray, in *The Ti-V (Titanium-Vanadium) system, Phase Diagrams of Binary Titanium Alloys*, ASM International (Metals Park, OH, 1987), pp. 319–27
- [49] Y.L. Xue, S.M. Li, H. Z. L.P. Li, H.Z. Fu, *Acta Metall. Sin. -Engl. Lett.* **58**, 514 (2015).
- [50] Y.W. Chen, Y.K. Li, X.W. Cheng, C. Wu, B. Cheng, Z.Q. Xu, *Materials* **11**, 208 (2018)
- [51] A.L. Yonkeu, I.P. Swainson, J. Dufour, J. Huot, *J. Alloys Compd.* **460**, 559 (2008)
- [52] H. Liang, Y.G. Chen, Y.G. Yan, C.L. Wu, M.D. Tao, M.J. Tu, *Rare Metal Mater Eng.* **35**, 1375 (2006)
- [53] G. Ek, Ø.S. Fjellvåg, P. Vajeeston, J. Armstrong, M. Sahlberg, U. Häussermann, *J. Alloys Compd.* **887**, 160320 (2019)
- [54] C. Zhang, Y. Wu, L. You, X.Z. Cao, Z.P. Lu, X.P. Song, *J. Alloys Compd.* **781**, 613 (2019)
- [55] M. Kitada, *J. Japan Inst Met.* **41**, 412 (1977)
- [56] M. Martin, C. Gommel, C. Borkhart, E. Fromm, *J. Alloys Compd.* **238**, 193 (1996)
- [57] E. Téliz, M. Abboud, R. Faccio, M. Esteves, F. Zinola, V. Díaz, *J. Electroanal. Chem.* **879**, 114781 (2020)
- [58] P. Ruz, V. Sudarsan, *J. Alloys Compd.* **627**, 123 (2015)
- [59] T.I. Bratanich, S.M. Solonin, V.V. Skorokhod, *Int. J. Hydrogen Energy* **20**, 353 (1995)
- [60] Y.G. Yao, Z.N. Huang, P.F. Xie, S.D. Lacey, R.J. Jacob, H. Xie, F.J. Chen, A.M. Nie, T.C. Pu, M. Rehwoldt, D.W. Yu, M.R. Zachariah, C. Wang, R.S. Yassar, J. Li, L.B. Hu, *Science* **359**, 1489 (2018)
- [61] J. Montero, G. Ek, L. Laversenne, V. Nassif, G. Zepon, M. Sahlberg, C. Zlotea, *J. Alloys Compd.* **835**, 155376 (2020)
- [62] H. Shen, J. Hu, P. Li, G. Huang, J. Zhang, J. Zhang, Y. Mao, H. Xiao, X. Zhou, X. Zu, X. Long, S. Peng, *J. Mater. Sci. Technol.* **55**, 116 (2020)
- [63] S. Fujitani, I. Yonezu, T. Saito, N. Furukawa, E. Akiba, H. Hayakawa, S. Ono, *J. Less-Common Met.* **172**, 220 (1991)
- [64] H.Z. Hu, C.M. Ma, Q.J. Chen, *J. Alloys Compd.* **877**, 160315 (2021)
- [65] S. Kumar, A. Jain, T. Ichikawa, Y. Kojima, G.K. Dey, *Renew. Sustain. Energy Rev.* **72**, 791 (2017)
- [66] T. Matumura, H. Yukawa, M. Morinaga, *J. Alloys Compd.* **284**, 82 (1999)
- [67] M. Ismail, M.S. Yahya, N.A. Sazelee, N.A. Ali, F.A. HalimYap, N.S. Mustafa, *J. Magnes. Alloy.* **8**, 832 (2020)
- [68] W. Zhang, P.K. Liaw, Y. Zhang, *Sci. China Mater.* **61**, 2 (2018)